Improved Background Rejection in Neutrinoless Double Beta Decay Experiments with Gaseous Xenon Detectors

A. Author[a]**, B. Author**[a*] **and C. Author**[b]

[a]*Instituto de Física Corpuscular (IFIC), CSIC & Universitat de València,*
  Calle Catedrático José Beltrán, 2, 46980 Paterna, Valencia, Spain
[b]*Name of Institute,*
  Address, Country
  E-mail: `CorrespondingAuthor@email.com`

ABSTRACT: We propose a potential improvement in background rejection capability of neutrinoless double-beta ($0\nu\beta\beta$) decay experiments conducted with high-pressure gas detectors capable of imaging electron tracks. The improvement relies on the ability to distinguish the different track signatures left by single-electron (background) events and two-electron ($0\nu\beta\beta$) events in such a detector in the presence of an external magnetic field. This initial study shows that, by analyzing the curvature of the reconstructed helical tracks, a potentially significant additional background rejection factor can be obtained with an acceptable loss in signal efficiency.

KEYWORDS: Neutrinoless double beta decay; Kalman filter; particle tracking.

---

*Corresponding author.

Contents

1. Introduction

Double beta decay refers to one of two processes in which two simultaneous β-decays occur within a nucleus and may be an accessible mode of decay in candidate isotopes for which the single-beta decay mode is forbidden or highly suppressed due to the energetics of the relevant nuclear configurations. In one such process referred to as two-neutrino double-beta decay, two electrons are emitted along with two antineutrinos,

$$(Z,A) \rightarrow (Z+2,A) + 2e^- + 2\bar{\nu}_e. \tag{1.1}$$

This process is allowed in the Standard Model and has been observed in several nuclei. Double-beta decay has also been postulated to exist in the zero-neutrino mode, or neutrinoless double-beta ($0\nu\beta\beta$) decay, in which the two antineutrinos are not emitted as a product of the reaction and the total energy released in the decay, $Q_{\beta\beta}$, is given to the two electrons. The observation of $0\nu\beta\beta$ would have several significant implications in fundamental physics. The decay cannot occur unless the neutrino is a Majorana particle, that is, physically equivalent to its anti-particle. Majorana neutrinos would be evidence for new physics at an energy scale inversely proportional

to the neutrino masses, and their existence violates the conservation of total lepton number. Furthermore, lepton number violation combined with CP violation could explain the excess of matter over anti-matter present in the universe via the mechanism known as leptogenesis. $0\nu\beta\beta$ decay has been frequently revisited in reviews (see for example [1, 2, 3]).

Many experimental challenges accompany these far-reaching physics implications. No confirmed observation of $0\nu\beta\beta$ has yet been made, though it has received much recent experimental attention. The current generation of experiments operate with tens to several hundred kilograms of candidate isotope mass. Some of these experiments such as EXO [4, 5], GERDA [6, 7], and KamLAND-Zen [8, 9] are already running and have directly observed the $2\nu\beta\beta$ mode in their chosen candidate isotope and set new lower limits on the half-life for $0\nu\beta\beta$ decay. Others are still in the prototype or construction phases including CUORE [10], MAJORANA [11], NEXT [12], SNO+ [13], and SuperNEMO [14]. Because no signal has yet been seen in experiments employing hundreds of kilograms of candidate isotope, it may be necessary to design a low-background experiment capable of operating with tonnes of candidate isotope to continue searching for the decay. The different technological strategies used in the current wide variety of $0\nu\beta\beta$ experiments may not be applicable at the tonne-scale, and such technologies would need to demostrate a clear ability to scale upward in size before being considered for a tonne-scale experiment.

2. Motivation

2.1 Background Rejection in Double-Beta Experiments

In recent $0\nu\beta\beta$ experiments, the total number of background events observed or expected in the energy region of interest has been on the order of a few counts to a few tens of counts per year. The NEXT experiment will use a high pressure xenon time projection chamber (TPC) to search for $0\nu\beta\beta$ decay using 100 kg of xenon enriched in the candidate isotope ^{136}Xe. The experiment currently expects a background rate of 5×10^{-4} counts/keV/kg/year, and for a 10 keV region of interest and 100 kg of isotope, 5 counts/year. To improve sensitivity at the current scale and in anticipation of a larger mass detector, we ask if this rate could possibly be reduced further. One potential improvement would be in energy resolution, narrowing the energy region of interest and therefore the total background rate. Xenon has been shown to have very good intrinsic energy resolution in the gas phase [15], and the current energy resolution achieved in NEXT prototypes using the low-noise electroluminescent (EL) gain process has not yet reached the intrinsic level [16]. Improvements particularly in photon collection and detection statistics could further improve the energy resolution and therefore the observed background rate in high pressure xenon TPCs.

The present study will focus on a different approach to background rejection in which the one-electron background events and two-electron double beta events are distinguished by examining the signature of the track left by the event in the detector. The energetic electrons produced in $0\nu\beta\beta$ decay deposit their energy as they travel through the xenon gas, leaving a track of ionization in their path. Because the ionization density dE/dx is greater at lower electron energies, the two ends of the electron tracks are marked by two "blobs" of greater ionization density. For a single-electron track, only one ionization track with one "blob" is produced. This difference in track signatures can be used to distinguish between background events, for example due to high-energy gamma rays,

that produce single-electron tracks, and double-beta events.[1] Such studies based on identification of the two "blobs" have already shown that the track signatures can be used to reject background events. In this study we compare the single and double-electron track signatures in the presence of an applied external field and quantify the additional ability to reject single-electron events that is gained by examining the curvature of the tracks induced by the field.

We note that the ability to conduct a detailed study of the reconstructed track is highly dependent on the resolution with which the track can be reconstructed in the detector. One major limiting factor in tracking resolution is the diffusion of electrons in the gas. The ionization track produced in some active volume must be drifted to a readout plane and therefore the electrons may diffuse significantly and limit the resolution with which the track can ultimately be reconstructed. In some cases use of an additive quenching gas may serve to reduce the diffusion to a level that would allow good resolution of the helical motion of an electron track in a magnetic field. In this study, we will examine the effectiveness of background rejection using track analysis in the presence of a magnetic field in the case of two different gases, xenon and selenium hexafluoride (SeF_6).

2.2 Particle Tracks in Xenon in a Magnetic Field

A particle of charge q moving at a velocity $\mathbf{v}$ in the presence of a magnetic field $\mathbf{B}$ is acted upon by a force

$$\mathbf{F} = q(\mathbf{v} \times \mathbf{B}). \tag{2.1}$$

This force will cause an electron to execute helical motion in the magnetic field such that if the thumb of the right hand is positioned along the direction of the field line $\mathbf{B}$ the electron will spiral in the direction in which the fingers curl when closed around the field line (see figure 1). The frequency of rotation about the field line is known as the cyclotron frequency $\omega_{cyc} = qB/m$, where B is the magnitude of the applied magnetic field $B = |\mathbf{B}|$ and m is the mass of the charged particle.
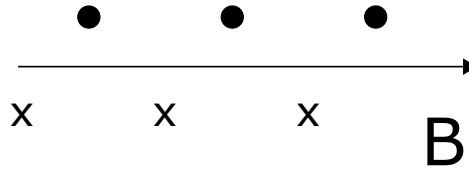

Figure 1. Motion of an electron in a magnetic field. The electron exhibits helical motion around the field line as shown (entering the page at the $\times$ and exiting the page at the $\bullet$) regardless of the direction of the component of the electron's velocity along the direction of $\mathbf{B}$.

In the presence of an applied external magnetic field, the ionization track produced by an energetic electron moving through high pressure xenon gas will be a helix with some alterations due to electron multiple scattering. If the direction of the applied magnetic field is known, the curvature of the track can be calculated to determine whether the component of the electron velocity along the magnetic field is parallel or antiparallel to the field. Assuming that the magnetic field is directed

---

[1]Note that this track signature is present for both $0\nu\beta\beta$ and $2\nu\beta\beta$ events, and so it cannot be used to reject background events from the two-neutrino mode. For this one must rely on good energy resolution.

along the z-axis, we are interested in the curvature of the track in the *x-y* plane as it progresses in *z*. The curvature κ in the *x-y* plane can be calculated for a track parameterized by the coordinate *z* as

$$\kappa = \frac{(dx/dz) \cdot (d^2y/dz^2) - (dy/dz) \cdot (d^2x/dz^2)}{\left[(dx/dz)^2 + (dy/dz)^2\right]^{3/2}}. \tag{2.2}$$

With this definition, an electron traveling in the direction of the magnetic field will spiral around the field lines with positive curvature, while an electron traveling opposite the direction of the magnetic field will spiral with negative curvature. The curvature, however, will be of the opposite sign if the track orientation is not properly identified in the calculation (i.e., if dz is of the wrong sign). Thus, when calculating the curvature of a single-electron track, one would expect $\kappa > 0$ for $dz > 0$ and $\kappa < 0$ for $dz < 0$ given that dz is always in the direction of the electron velocity. However, for a $0\nu\beta\beta$ track, taking one of the extremes to be the beginning of the track and the other to be the end will lead to a calculation of κ assuming the wrong track orientation for one of the two electrons, as the vertex at which the reaction occured is found somewhere on the interior of the track. Therefore one expects to find $\kappa < 0$ for $dz < 0$ and $\kappa > 0$ for $dz > 0$ for a significant fraction of the track. This difference in the behavior of the calculated curvature of reconstructed tracks will allow for the separation of single-electron and $0\nu\beta\beta$ events.

One serious limitation to this strategy is the presence of electron multiple scattering. This is the process by which an energetic electron is scattered repeatedly while traveling through the xenon gas and can result in deviations of its path by significant angles. The process can be modeled by, assuming the electron is traveling along an axis in the $\hat{\mathbf{z}}$ direction, considering the angle of deflection projected on the *x* and *y* planes when scattered through a thickness of xenon *x*. Each of these angles θ_x and θ_y can be modeled by a gaussian distribution as

$$\sigma^2(\theta_{x,y}) = \frac{13.6\,\text{MeV}}{\beta p} \sqrt{dz/L_0} \left[1 + 0.038\ln(dz/L_0)\right], \tag{2.3}$$

for an electron with momentum *p* in MeV/c before scattering and beta factor β (where $c = 1$). L_0 is the radiation length, a property of the medium. Without the influence of multiple scattering, the track of an energetic electron would follow a helical path with a well-defined curvature, apart from noise due to diffusion and the track reconstruction procedure. In this case the transverse momentum could be directly determined by the curvature as $p_T = -B/\kappa$, and a single-electron track for which the momentum is greatest at one end of the track and decreases toward the other end would be clearly distinguishable from a double-electron track consisting of two electrons traveling in opposite directions originating at some vertex in the middle of the track. However, due to multiple scattering, the magnitude of the curvature will be altered significantly. Therefore, in this study we use only information on the sign of the curvature, which, though it can still be affected by a scatter of sufficiently large angle, remains relatively intact despite multiple scattering.

2.3 Use of Selenium Hexafluoride as a Substitute for Xenon

The use of selenium hexafluoride (SeF_6) gas has recently been proposed (cite Dave) as an alternative to xenon for an ultra-low background $0\nu\beta\beta$ search experiment.

3. Implementation

3.1 Track Preparation

The simulation-based study consisted of analysis of Monte Carlo datasets generated in a large virtual box of high pressure gas using GEANT4. For various configurations of gas pressure and magnetic field, 10^4 events were generated consisting of single energetic electrons of kinetic energy equal to the Q-value of $0\nu\beta\beta$ in xenon gas ($Q_{\beta\beta} = 2.447$ MeV), and 10^4 $0\nu\beta\beta$ events were generated consisting of two energetic electrons with total energy equal to $Q_{\beta\beta}$. Each simulated track was recorded as a series of hits consisting of a location (x, y, z) and a deposited energy E. Before proceeding with further analysis, the summed energy of all hits recorded in the track was required to be at least 2.4 MeV (events in which significant energy escaped from the active volume in the simulation were not considered further).

From this series of hits, a single continuous track was constructed by defining a main track as those hits produced directly by the one (or two in the case of $0\nu\beta\beta$ events) energetic electron(s) produced in the event. Other hits produced by secondary ionization electrons were added to the main track if they were produced within 1 mm of at least one hit in the main track, and indirectly[2] if they were produced within 2 cm of at least one hit in the main track. Events containing hits located greater than 2 cm from all hits in the main track were discarded. Note that the ordering of the hits was determined by Monte Carlo, however the orientation of the track was defined by constructing two "blobs" composed of hits within 2 cm of the first and last hits of the track, and setting as the "initial" end the one at which the constructed blob had less total energy. The resulting list of hits was then smeared randomly in (x, y) about their original values according to a gaussian distribution with sigma σ_s. The hits were then "sparsed," that is each group of N_s hits was replaced with a single hit with (x, y, z) location equal to the energy-weighted average of the constituent hit locations and energy equal to the sum of the constituent energies. From this point on we will refer to the final list of ordered hits as the "track."

The x, y, and z-coordinates of the track are then separated into individual arrays, and a lowpass filter is applied to each array. This serves to smooth the track and facilitates the calculation of the derivatives. Figure 2 shows an example of a track before and after the filtering procedure, the details of which are discussed in appendix A.

3.2 Determination of the Track Curvature

The curvature at each hit in the track is calculated by numerical computation of the derivatives dx/dz, dy/dz, d^2x/dz^2, and d^2y/dz^2 using the values in the coordinate arrays. From these the curvature κ is calculated at each point. Since we do not have x and y as a function of z but rather x, y, and z as a function of hit number n, we can calculate the derivatives $x' \equiv dx/dn$, $y' \equiv dy/dn$, $z' \equiv dz/dn$ using the chain rule as $\frac{dx}{dz} = x'/z'$, and

$$\frac{d^2x}{dz^2} = \frac{x'' - z''(dx/dz)}{(z')^2}. \tag{3.1}$$

---

[2]Hits added indirectly were bunched into sub-tracks of hits lying within 1 mm of at least one other hit in the sub-track, and the energy-weighted centroid of the sub-track was calculated. The total energy of the sub-track was then added to the hit closest to the location of the calculated centroid.
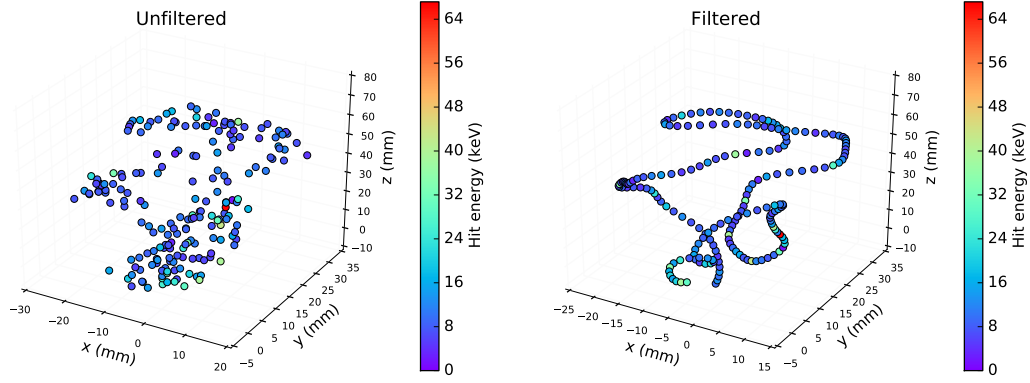
Figure 2. An example of a single-electron track before (left) and after (right) the application of a lowpass filter. The filter applied in this case is shown in appendix A in figure 9.

The expressions for dy/dz and d^2y/dz^2 can be obtained by replacing in the above $x \to y$. Note that outliers may need to be removed from the resulting arrays of first and second derivatives due to points between which the z-coordinate changes very little. To ensure more stable values of the derivatives, an outlier removal procedure is applied to all derivatives and second derivatives computed which consists of iteratively calculating the mean and variance σ of each array, replacing any value that lies outside of 5σ of the mean value with the average of the two nearest values in the array, and continuing this procedure until the calculated variance σ'^2 is no longer less than the previous value of the variance σ^2.

The curvature calculated using each pair of points is then corrected as follows: if for the two points $z_2 < z_1$, that is $dz < 0$, the curvature is multiplied by -1 (see section 2.2). Note that the outlier removal procedure described above is also applied to the calculated curvature array.

3.3 Background Rejection

The rejection of background events is performed by condensing the curvature information for each track into a single numerical value indicative of the nature of the track (signal or background). First a curvature sign array is created consisting of values of either $+1$ or -1 depending on the sign of each value in the calculated curvature array. The numerical value, which we will call the curvature asymmetry factor, is defined as the average of the curvature sign array using elements in the first half of the track minus the average of the curvature sign array using elements in the second half of the track.

$$\phi_C = \frac{1}{N/2}\left(\sum_{i=0}^{N/2-1} \text{sgn}(\kappa_i) - \sum_{i=N/2}^{N} \text{sgn}(\kappa_i)\right). \tag{3.2}$$

Note that if the number of hits in the track is odd, the first term includes the first $(N-1)/2$ hits and the second term includes the remaining $(N-1)/2+1$ hits. Though due to multiple scattering and imperfect reconstruction resolution, this factor is not a perfect discriminator, statistically it can be used to separate single-electron and double-beta events.

To further illustrate this idea, we consider a simple Monte Carlo in which tracks are generated in steps of 10 keV energy deposition using the NIST dE/dx curve and equation 2.3 to model

multiple scattering. For each energy deposition $\Delta E = 10$ keV, the electron is propagated along a path calculated according to the force exerted by the magnetic field (equation 2.1) of length $\Delta x = \int_E^{E-\Delta E}(dE/dx)^{-1}dE$. The initial direction of travel is assigned at random and is updated after each step Δx by calculating a random θ_x and θ_y using equation 2.3 and assuming the direction of travel is along the z-axis. A single-electron track is generated in this way assuming an initial energy of 2.447 MeV, to simulate background events. For "signal" events, two single-electron tracks are generated from a common vertex, each with an initial energy of $2.447/2 = 1.2235$ MeV.

This simplified Monte Carlo allows us to study the influence of multiple scattering present in the simulated events in a straightforward manner by changing the prefactor in equation 2.3 from 13.6 MeV to a lower value. Figure 3 shows several signal and background tracks and their calculated curvature sign simulated with different multiple scattering prefactors corresponding to no multiple scattering (0 MeV), the standard amount of multiple scattering (13.6 MeV). and double the standard amount of multiple scattering (27.2 MeV).

Increased multiple scattering makes the background rejection procedure more difficult, as the random motion of multiple scattering often works against the curvature introduced by the magnetic field and quantified in equation 3.2. Figure 4 shows the calculated asymmetry factors for 1000 single-electron and two-electron tracks produced with different amounts of multiple scattering introduced. Note that other factors also affect the ability to reject background based on the asymmetry factor. In this simple model, two-electron tracks are produced for which both electrons are given exactly half of the energy $Q_{\beta\beta}$, though in practice, the energy will not be shared equally. This serves to weaken the background rejection power of the asymmetry factor because the point at which the track should be separated is not always the central point. The position reconstruction resolution, which is assumed to be perfect in this simple model, in practice will not be perfect and will also serve to weaken the background rejection power. Furthermore, the multiple scattering model used only allows for scattering angles chosen from a Gaussian distribution with variance dictated by equation 2.3 and does not model the non-Gaussian (large-angle) scattering that can occur in practice.[3] These factors are taken into account in the results of the more detailed Monte Carlo study presented in section 4.

4. Results

4.1 Background Rejection in Xenon

The analysis described in section 3 was performed for single-electron and $0\nu\beta\beta$ tracks for all combinations of $P = 5$, 10, and 15 atm and $B = 0.1$, 0.3, 0.5, 0.7, and 1.0 T. In all of these configurations, the hits were smeared in (x, y) with $\sigma_s = 2$ mm and sparsed with $N_s = 2$. Additional analyses in the $P = 10$ atm, $B = 0.5$ T configuration were performed, one with $\sigma_s = 1$ mm and $N_s = 1$, and another with $\sigma_s = 3$ mm and $N_s = 3$. For each configuration, 10^4 events of each track type (single-electron and $0\nu\beta\beta$) were generated, and approximately 40-65% of the tracks passed the initial topological cuts described in section 3.1. Figure 5 shows the calculated curvature signs

---

[3]The absence of non-Gaussian scattering is a reasonable explanation for why the standard amount of multiple scattering dictated by equation 2.3 does not yield tracks that qualitatively match those of more complex simulations (compare figures 3 and 5).
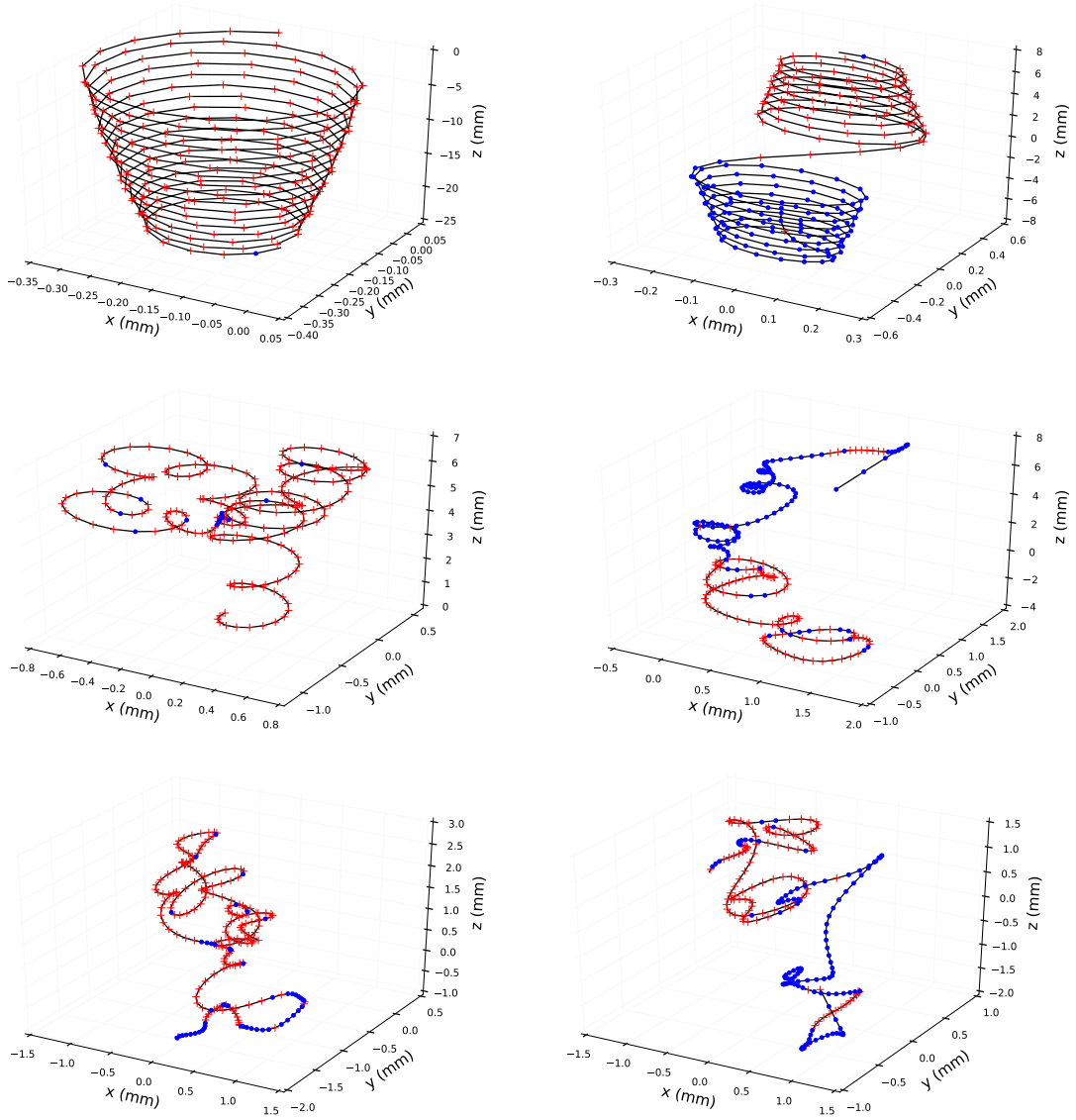
Figure 3. Calculated curvature sign at each point along the track for a single-electron event (left) and a double-beta event (right). The tracks were generated with no multiple scattering (top), the standard amount of multiple scattering (middle). and double the standard amount of multiple scattering (bottom). The red + markers indicate positive curvature, while the blue dots indicate negative curvature.

for a single-electron and double-beta event, after filtering with a lowpass filter, at $B = 0.5$ T and $P = 10$ atm. Note that these tracks qualitatively better resemble those produced in the simple Monte Carlo with double the standard strength of multiple scattering, meaning that the model based on equation 2.3 somewhat underestimates the effects of multiple scattering.

The asymmetry factor shown in equation 3.2 was calculated for these tracks, and a cut was placed on the calculated asymmetry factors defining the events considered to be candidate $0\nu\beta\beta$ tracks. The cut was varied, and in each case the fraction of single-electron (background) tracks
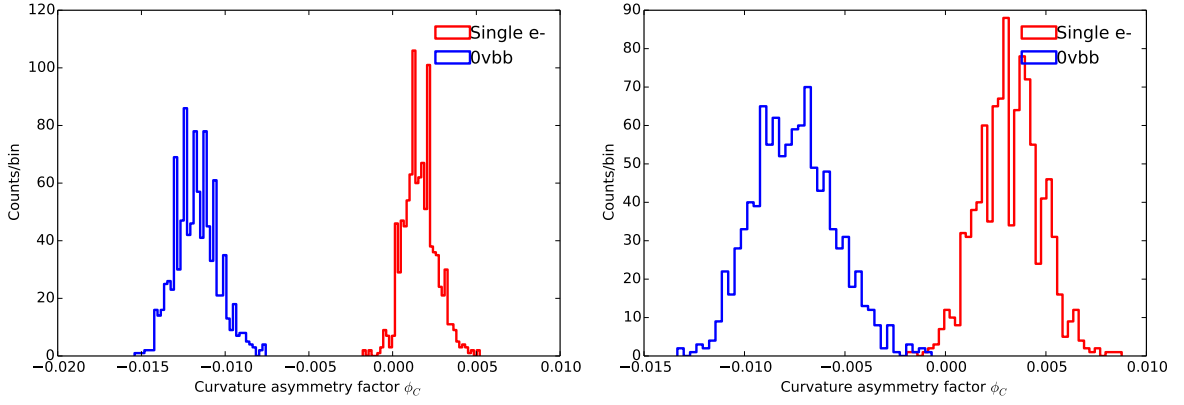
Figure 4. Asymmetry factors calculated for 1000 single-electron and double-electron tracks generated with the standard amount of multiple scattering (left) and twice the standard amount of multiple scattering (right). Note that though the background rejection capability appears almost perfect based on the results of this simple Monte Carlo, other factors such as the reconstruction resolution and non-equal energy sharing between the two electrons in $0\nu\beta\beta$ decay degrade the discrimination power and are not taken into account here.
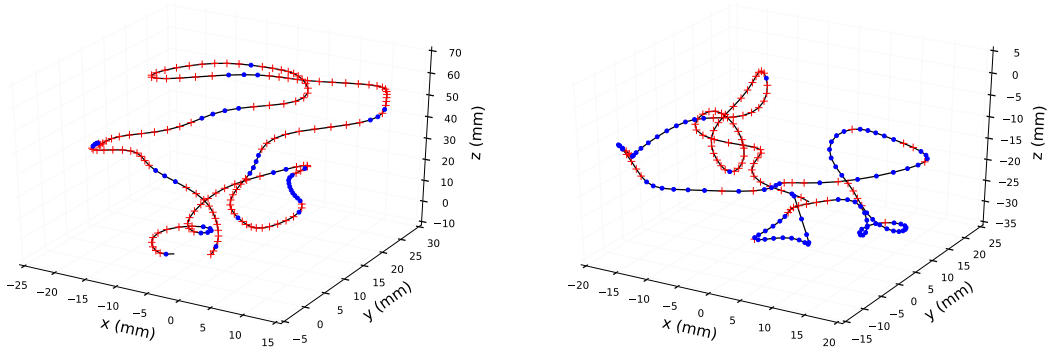

Figure 5. Calculated curvature sign at each point along the track for a single-electron event (left) and a double-beta event (right) generated using the GEANT-based Monte Carlo. The red + markers indicate positive curvature, while the blue dots indicate negative curvature. Note that a lowpass filter has been applied to the tracks shown as described in section **??**.

rejected by the cut was determined along with the fraction of $0\nu\beta\beta$ (signal) tracks accepted.[4] An example of such an analysis is summarized in figure 6.

To demonstrate the performance of the method at the different configurations of gas pressure and magnetic field, we examine the signal efficiency s (fraction of $0\nu\beta\beta$ events correctly identified) obtained given a cut that provides approximately 80% and 90% background rejection. The results are shown in figure 7. Note that in all of these analyses the lowpass filter applied to the track was designed with a fixed cutoff frequency of $k_{\text{cyc}} = 0.085$, as a fixed cutoff frequency was found to produce overall better results than one calculated on a track-by-track basis (see appendix A).

---

[4]This is the fraction of the events that passed the initial topological analysis. That is, we are considering the additional background rejection provided by this analysis once events of the chosen energy with a single continuous track have been selected out.
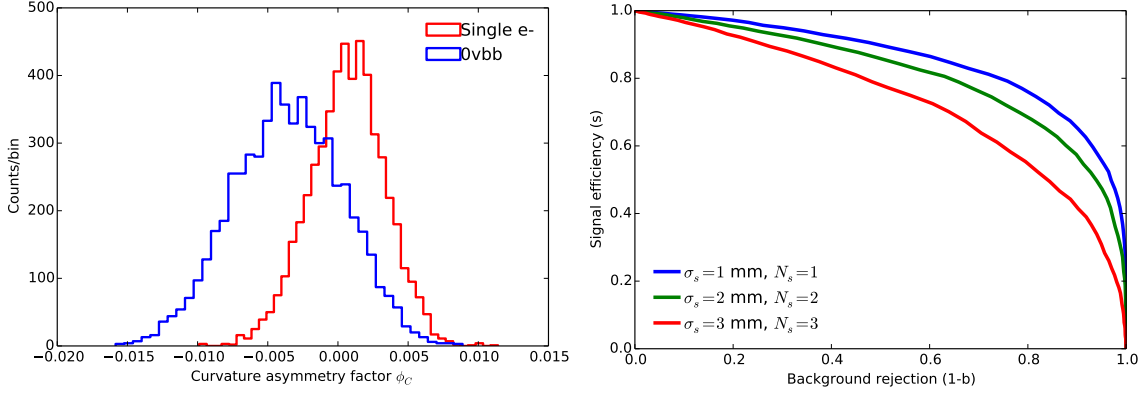
Figure 6. Curvature asymmetry factor for single-electron and $0\nu\beta\beta$ events with $\sigma_s = 2$ mm and $N_s = 2$ (left) and resulting signal efficiency vs. background rejection curve produced by varying a cut on ϕ_C space, shown also for $\sigma_s = 1$ mm and $N_s = 1$ and $\sigma_s = 3$ mm and $N_s = 3$ (right). Here s is the fraction of the total number of $0\nu\beta\beta$ events considered that was identified as a $0\nu\beta\beta$ event, and b is the fraction of the total number of single-electron background events considered that was identified as a $0\nu\beta\beta$ event. These results were obtained for the $P = 10$ atm and $B = 0.5$ T configuration.
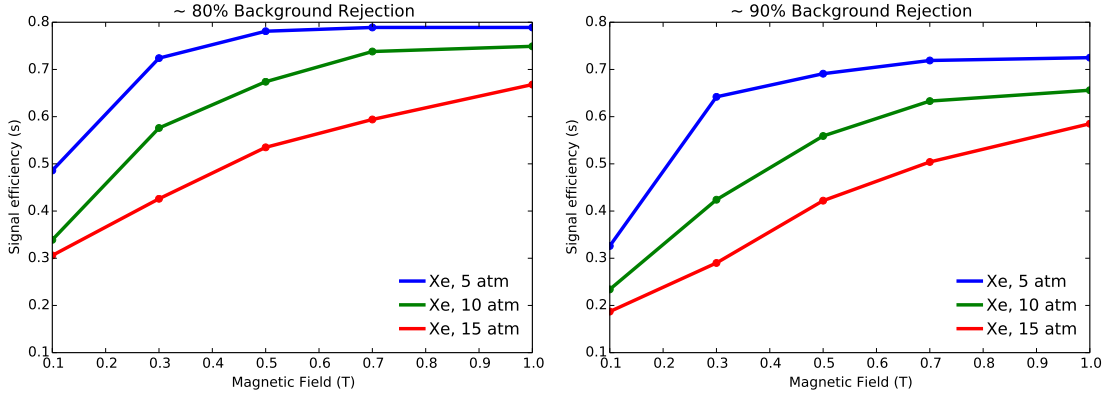

Figure 7. Signal efficiency corresponding to approximately 80% background rejection (left) and 90% background rejection (right) vs. magnitude of applied external magnetic field for different pressures. In this analysis, k_{cyc} was fixed to a value of 0.085, a value representative of these simulated tracks for $B = 0.5$ T.

4.2 Comparison to Performance in SeF$_6$

Comparing the performance of xenon to that of SeF$_6$, we ultimately find that the performance is similar, and therefore that the additional challenges associated with constructing a TPC based on SeF$_6$ would not be worth the benefits in performance, if any.

5. Conclusions

The application of an external magnetic field in a high-pressure xenon detector capable of particle track reconstruction with resolution of approximately 2 mm in (x, y, z) could present an additional background rejection factor of 80% with an acceptable loss of signal efficiency at pressures of about 10 atm or less. The background rejection improves with decreasing pressure due to the
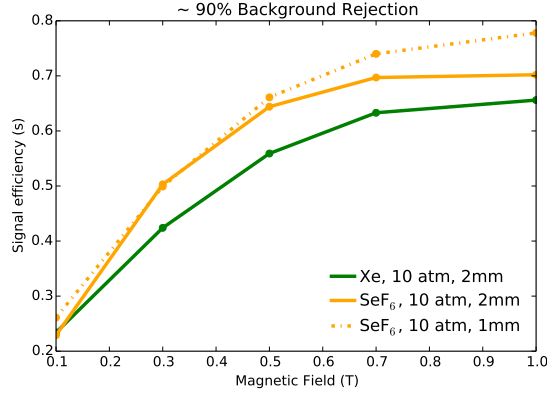
Figure 8. Signal efficiency vs. magnetic field for 80% background rejection for 10 atm xenon (same as Xe 10 atm curve in figure 7 left) and for 10 atm SeF$_6$. Despite the reduced multiple scattering in SeF$_6$, the performance is not significantly different from that of pure xenon.

more extended tracks produced at lower gas densities. For the lower pressures (5 atm and 10 atm), relatively little increase in signal efficiency is gained for an increase in magnetic field for fields greater than approximately 0.5 T.

Even an 80% reduction in background would reduce the expected background rate in the NEXT experiment to 1×10^{-4} counts/keV/kg/year, or about 1 count/year for a 100 kg detector. This warrants further investigation, including the development of a discriminating variable more sophisticated than the asymmetry factor used in this study and application of this methodology to Monte Carlo data generated taking into account more aspects of the detector track reconstruction process.

A. A Lowpass FIR Filter

One way to make the calculation of the curvature of a track less susceptible to noise introduced through multiple scattering and non-ideal reconstruction resolution is to apply a lowpass filter to the lists of values for each coordinate x, y, and z. We now look at the arrays of x, y, and z coordinates as digital signals in the time domain, e.g. $x[n]$, where n is the index of the corresponding hit. Each array can be represented in the frequency domain $X[k]$ using the discrete Fourier transform

$$X[k] = \sum_{n=0}^{N-1} x[n]e^{-i2\pi kn/N}, \tag{A.1}$$

where N is the total number of samples and k is the discrete frequency of each complex sinusoid $e^{-i2\pi kn/N}$ in cycles per N samples. This discrete frequency can be translated to an analog frequency f_k (for example in units of time^{-1}) by knowing the frequency at which the digital signal was sampled, or the sampling frequency f_s in samples per unit time, as

$$f_k = kf_s. \tag{A.2}$$

The goal is to apply a digital lowpass filter to the coordinate arrays that serves to smooth the track by eliminating high-frequency noise yet retains the curvature of the track due to the magnetic

field. The ideal lowpass filter will serve to eliminate sinusoidal components $X[k]$ in the digital signal for k greater than some cutoff frequency k_c and allow others with k less than k_c. In practice, the filter will have a non-ideal stopband in which sinusoidal components with frequencies less than k_c will be increasingly preserved with decreasing k and those with frequencies greater than k_c will be increasingly attenuated with increasing k. The filter must be designed to ensure we don't eliminate the sinusoidal motion introduced by the magnetic field, and we use a filter with a wide stopband (this reduces its complexity) and place k_c near the discrete frequency corresponding to the cyclotron frequency

$$\omega_{\text{cyc}} = qB/m_e = 1.76B \times 10^{11} \text{ rad/s,} \tag{A.3}$$

where $q \approx -1.60 \times 10^{-19}$ is the electron charge in Coulombs, B is the magnetic field strength in Tesla, and $m_e \approx 9.11 \times 10^{-31}$ is the electron mass in kg. The filter will be a finite impulse response (FIR) filter and will take the form of a list of coefficients b_m. It is applied to the signal $x[n]$ as

$$x_f[n] = \sum_{m=0}^{N_f} b_m x[n-m] \tag{A.4}$$

where the number of filter coefficients N_t is the order of the filter. A delay will exist in the final filtered signal equal to $N_t/2$ samples, and the final $N_t/2$ samples will not be useful in the final analysis and are removed. For a track sampled in x, y, and z for a total of N samples, to determine what discrete frequency k_{cyc} to which this analog frequency ($\omega_{\text{cyc}}/2\pi$ in cycles per second) corresponds, one must know the frequency with which the track has been sampled. An average track production time $\overline{T}$ can be calculated from tabulated values of dE/dx (which, since this refers to kinetic energy loss, we will call dK/dx) as

$$\overline{T} = \frac{1}{c} \int_0^{K_f} \left[\frac{\sqrt{(K^2 - m_e^2)}}{K + m_e} (dK/dx) \right]^{-1} dK \approx 1.25 \text{ ns,} \tag{A.5}$$

where here we have used $K_f = Q_{\beta\beta} = 2.447$ MeV and tabulated dE/dx from NIST [17] in xenon. The sampling frequency is then $f_s = N/T$, and so the motion due to the magnetic field should manifest itself in the arrays of sampled x and y coordinates of the track as a sinusoidal component of discrete frequency

$$k_{\text{cyc}} = (qB/m) \cdot (\overline{T}/N). \tag{A.6}$$

One should ensure that the track is sampled at a rate higher than the cyclotron frequency, that is $N/T > \omega_{\text{cyc}}/2\pi$, or the helical motion will not be properly reconstructed. An example filter is shown in figure 9. For each track, an FIR filter is designed with stopband frequency equal to $1.2k_{\text{cyc}}$ and stopband width equal to 0.2. This was sufficient to eliminate high-frequency noise, leaving a smooth track for the calculation of derivatives, yet the filter order was low enough so as to not lose a significant number of the track samples. For this track, a number of samples $N = 198$ and using $T = 1.25$ ns from equation A.5 and $\omega_{\text{cyc}} = 0.88 \times 10^{11}$ rad/s from equation A.3 with $B = 0.5$ T, we have $k_{\text{cyc}}/2\pi = 0.089$ cycles/sample as shown in figure 9.
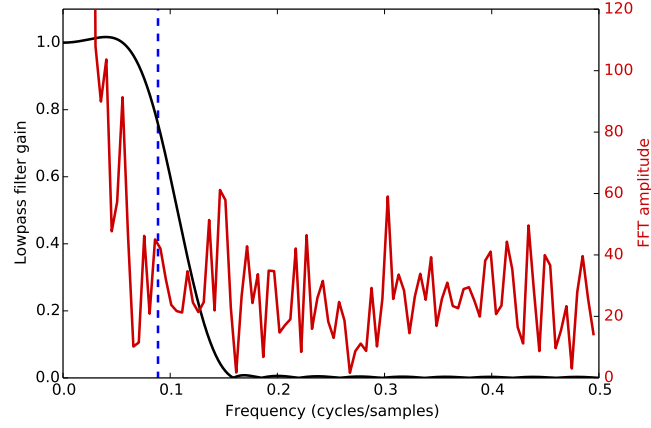
Figure 9. FIR filter gain vs. discrete frequency k (solid black curve) designed for a track of length $N = 198$ samples. The coefficients $X[k]$ of the fast fourier transform (FFT) of the x-coordinate array of the track are shown vs. discrete frequency in gray. The cutoff frequency used in designing the filter is shown as a blue vertical line. The filter serves to eliminate the high-frequency noise components of the track that make the calculation of derivatives more difficult.

As the magnitude of B increases, the frequency of helical motion often becomes great enough that placing the filter cutoff frequency k_c near the cyclotron frequency does not permit sufficient filtering of the high-frequency components of the track, and the resulting track is not smooth enough for a clean calculation of the curvature. Therefore it may be an advantage to place the cutoff frequency of the filter below k_{cyc} despite increased attenuation at the discrete frequency corresponding to the helical motion induced by the magnetic field.[5] Figure 10 shows the signal efficiency vs. magnetic field for a background rejection of 90% at 10 atm in pure xenon for which the filter was designed for each track individually with cutoff frequency equal to k_{cyc}, and for which the cutoff frequency of all filters was chosen to be a fixed value. Because the fixed-cutoff analysis performs significantly better at higher fields, it was chosen as the primary analysis in this study.

Acknowledgments

References

[1] J. J. Gómez-Cadenas, J. Martín-Albo, M. Mezzetto, F. Monrabal, and M. Sorel. The search for neutrinoless double beta decay. *Riv. Nuovo Cim.*, 35:29–98, 2012.

---

[5]In any case, to the constant diversion from the ideal path of the electron introduced by multiple scattering, the curvature of the track in the magnetic field will not appear at a single distinct value in the frequency domain.
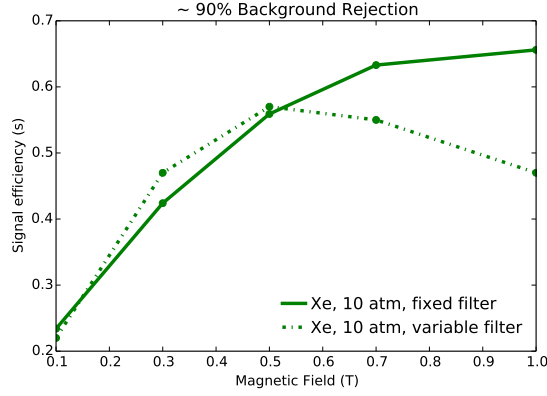
Figure 10. Signal efficiency vs. magnetic field for 90% background rejection shown with two different filter calculations to demonstrate the effect of the lowpass filter design on the background rejection performance. The use of a filter with cutoff frequency calculated on a track-by-track basis ("variable filter") does not yield a remarkable improvement in performance at low values of B and allows too much noise to remain at high values of B. The use of a filter with a fixed cutoff frequency ("fixed filter," same as Xe 10 atm curve in figure 7 left) in the range of those calculated for $B = 0.5$ T for all tracks eliminates the noise but does not eliminate information about the curvature to the extent that the performance is degraded.

[2] S. Bilenky. Neutrinoless double beta-decay. *Physics of Particles and Nuclei*, 41:690–715, 2010.

[3] Steven R. Elliott. Recent Progress in Double Beta Decay. *Mod. Phys. Lett. A*, 27:1230009, 2012.

[4] M Auger et al. The EXO-200 detector, part I: detector design and construction. *JINST*, 7: P05010, 2012.

[5] M. Auger et al. Search for Neutrinoless Double-Beta Decay in Xe136 with EXO-200. *Phys. Rev. Lett.*, 109:032505, 2012.

[6] I. Abt et al. A New ^{76}Ge Double Beta Decay Experiment at LNGS. *arXiv:hep-ex/0404039*, 2004.

[7] M. Agostini et al. Results on Neutrinoless Double-β Decay of ^{76}Ge from Phase I of the GERDA Experiment. *Phys. Rev. Lett.*, 111:122503, 2013.

[8] A. Gando et al. Measurement of the double-β decay half-life of ^{136}Xe with the KamLAND-Zen experiment. *Phys. Rev. C*, 85:045504, 2012.

[9] A. Gando et al. Limit on Neutrinoless $\beta\beta$ Decay of ^{136}Xe from the First Phase of KamLAND-Zen and Comparison with the Positive Claim in ^{76}Ge. *Phys. Rev. Lett.*, 110:062502, 2013.

[10] D. R. Artusa et al. Searching for neutrinoless double-beta decay of ^{130}te with cuore. *Advances in High Energy Physics*, 2015:879871, 2015.

[11] N. Abgrall et al. The Majorana Demonstrator Neutrinoless Double-Beta Decay Experiment. *arXiv:1308.1633*, 2013.

[12] J.J. Gómez Cadenas et al. Present Status and Future Perspectives of the NEXT Experiment. *Advances in High Energy Physics*, 2014:907067, 2014.

[13] S. Biller. SNO+ with Tellurium. *arXiv:1405.3401*, 2014.

[14] R. Arnold et al. Probing new physics models of neutrinoless double beta decay with SuperNEMO. *Eur. Phys. J. C*, 70:927–943, 2010.

[15] A. Bolotnikov and B. Ramsey. The spectroscopic properties of high-pressure xenon. *Nucl. Instrum. Methods A*, 396:360–370, 1997.

[16] V. Álvarez et al. Near-intrinsic energy resolution for 30–662 keV gamma rays in a high pressure xenon electroluminescent TPC. *Nucl. Instrum. Methods A*, 708:101–114, 2013.

[17] J. H. Hubbell and S. M. Seltzer. *NIST: Tables of X-Ray Mass Attenuation Coefficients and Mass Energy-Absorption Coefficients*. http://physics.nist.gov/PhysRefData/XrayMassCoef/tab1.html.